Journal of Power Sources 559 (2023) 232632

Contents lists available at ScienceDirect

Journal of Power Sources

journal homepage: www.elsevier.com/locate/jpowsour

Porous nanofibers comprising VN nanodots and densified N-doped CNTs as redox-active interlayers for Li–S batteries

Jang Min Choi[1], Rakesh Saroha[1], Ji Soo Kim, Mi Rim Jang, Jung Sang Cho*

Department of Engineering Chemistry, Chungbuk National University, 1, Chungdae-Ro, Seowon-Gu, Cheongju-Si, Chungbuk, 361-763, Republic of Korea

HIGHLIGHTS

- Hierarchically porous nitrogen-doped carbon (P–N–C) nanofibers are prepared.
- Comprising VN nanodots and densified entangled N-doped CNTs (N-CNTs).
- VN nanodots act as chemisorption sites for efficient anchoring of lithium polysulfide.
- N-CNTs increase the overall conductivity of the nanostructure framework.
- Li–S cell with P–N–C@VN/N-CNT NF-coated separator exhibits stable performance.

GRAPHICAL ABSTRACT

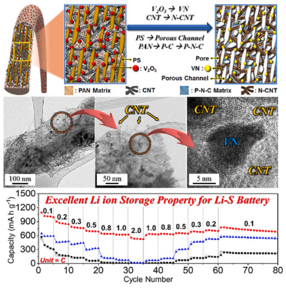

ARTICLE INFO

Keywords:
Electrospinning
N-doped C fibers
Metal-nitride nanodots
N-doped carbon nanotubes
Multifunctional interlayer

ABSTRACT

A synthesis strategy to obtain hierarchically porous N-doped carbon (P–N–C) nanofibers (NFs) comprising VN nanodots and highly densified-entangled N-doped CNTs (N-CNTs) was visualized. The unique redox-active nanostructure was applied as a multifunctional interlayer for highly stable Li–S batteries (LSBs). The P–N–C skeleton obtained *via* selective removal of amorphous carbon (AC) and polystyrene (PS) not only guarantees efficient electrolyte percolation but also facilitates rapid diffusion of charged species during charge-discharge processes. Moreover, the N-CNTs constituting the fiber matrix increase the overall conductivity of the framework. Besides, highly conductive vanadium nitride (VN) nanodots act as chemisorption sites for efficient lithium polysulfide capturing and prohibit their diffusion towards the anode through efficient catalytic conversion, thus improving the elemental S utilization. The Li–S cells utilizing P–N–C@VN/N-CNT NF as a multifunctional barrier resulted in decent rate capabilities (559 mA h g^{-1} at 2.0 C) and long-term cycling stabilities at low and high C-rates (432 mA h g^{-1} after the 400th cycle at 0.1 C and 290 mA h g^{-1} at the end of 600th cycle at 1.0 C). This is attributed to the combined synergistic effects of the P–N–C framework, N-CNT matrix, and polar VN nanodots.

1. Introduction

Since its launch, lithium-ion battery (LIB) technology has dominated the commercial market and become the preferred candidate for compact electronics and automobiles such as electric vehicles [1–4]. However, the present LIB technology's gravimetric and volumetric energy densities approach their theoretical limit [5,6]. Achieving higher gravimetric (~500 W h kg^{-1}) and volumetric energy densities (>1000 W h

---

* Corresponding author.
E-mail address: jscho@cbnu.ac.kr (J.S. Cho).

[1] These authors contributed equally.

https://doi.org/10.1016/j.jpowsour.2023.232632
Received 12 September 2022; Received in revised form 5 December 2022; Accepted 3 January 2023

L^{-1}) remains a challenge for the research community. Lithium–sulfur (Li–S) batteries have long been considered promising alternatives to state-of-the-art LIBs owing to their ultra-high theoretical energy densities (~2600 W h kg^{-1} or 2800 W h L^{-1}) [7–9]. In addition, a high theoretical capacity (1675 mA h g^{-1}), considerable discharge potential (~2.1 V *vs.* Li/Li^+), and abundance of S make Li–S battery (LSB) technology a highly promising rechargeable storage system [10,11]. However, widescale commercial use of LSBs is hindered by a few intrinsic shortcomings such as the electrically and ionically insulating nature of elemental S and discharge product (low-order insoluble lithium polysulfide i.e., Li_2S), diffusion and migration of extremely soluble higher or middle-order lithium polysulfide (LiPS) *via* well-known "shuttle effect", and severe volume variations during redox process (~80%) due to the large density difference between S and Li_2S [12–16].

Extensive research efforts have been put by the research fraternity in the last two decades to address the above-discussed issues by various means such as encapsulating S inside various porous matrices [17–21], constructing advanced S composite materials using different polar materials for prohibiting shuttling effect [22–25], controlling deposition of Li_2S [26], and protection of Li anode using electrolyte optimization [27]. In addition, a new strategy for introducing modified cell components has gained momentum in the last few years. The modified cell component, or "functional interlayers", usually consists of a thin coating of polar materials like metal oxides [9,28–31], metal selenides/sulfides [32–34], metal nitrides [35,36]; highly conductive carbon skeleton [37–42], and many more [43–45], which act as chemisorption sites for capturing dissolved LiPS species and allows their smooth conversion to S-like species. However, the coated material must be highly conductive to guarantee a fast charge transfer process, adequately porous to accommodate the volume variations during the redox process, and contain polar materials for chemical absorption of LiPS, thereby weakening the shuttle effect [46].

In this regard, the utilization of a one-dimensional (1-D) hierarchically porous and highly conductive framework as a redox-active skeleton and interlayer material is envisioned in the present work. For the 1-D nanostructure, the conventional electrospinning technique was employed. The nanofiber mat consisted mainly of polyacrylonitrile (PAN)-derived nitrogen-doped carbon (N-doped C) nanofibers (NFs). N-doped C nanofibers were selected primarily because of their ease of synthesis and easily controllable parameters. Notably, the presence of N doping in the porous skeleton also contributes to the overall conductivity mainly due to the higher electronegativity of the N atom than that of C [47]. This will guarantee the fast redox reaction process *via* rapid charge transfer kinetics and therefore, enhance the electrochemical performance. In addition, porosity was introduced using oval-shaped polystyrene (PS) granules that stretched during electrospinning due to the applied electric field and subsequently resulted in the formation of tunnel-like long-range channels inside the N-doped C skeleton during high-temperature heating. Furthermore, to enhance the overall conductivity, highly densified-entangled N-doped carbon nanotubes (N-CNTs) were introduced due to their high electronic conductivity (~10^5 S cm^{-1}). Furthermore, as a polar material, vanadium nitride (VN) nanodots were introduced *via* a carbonitrothermic reduction process using vanadium pentoxide (V_2O_5) as a precursor. VN nanodots not only behave as trapping sites for LiPS anchoring but also guarantee the catalytic conversion of trapped polysulfides owing to their high electronic conductivity (~10^4 S cm^{-1}) [16]. Therefore, a well-designed porous and conductive nanostructure as an interlayer material could efficiently enhance the overall electrochemical properties of Li–S cells *via* synergetic effects between the porous structure, conductive channels, and polar material. The structural merits resulted in shortened diffusion length for Li–ions in addition to better electrolyte percolation or electrode wetting and channelizing the severe volume changes during lithiation and delithiation whereas the numerous conductive channels provided by N-doped C and N-CNTs support fast redox kinetics.

Benefitting from the novel nanostructure design strategy, the hierarchically porous and highly conductive N-doped C skeleton comprising highly densified-entangled N-CNTs and VN nanodots (abbreviated as "P–N–C@VN/N-CNT" NF) was visualized as multifunctional interlayers and polysulfide barrier to obtain highly stable Li–S batteries. The Li–S cells utilizing pure S electrodes and P–N–C@VN/N-CNT NF-coated separator as a polysulfide barrier exhibited decent rate capabilities along with prolonged stable cycling performance at various current rates. Therefore, we anticipate that the synthesis approach described in this work will add extensive knowledge to the current understanding of the development of advanced nanostructures for various energy-storage purposes.

2. Experimental

Sample preparation: The hierarchically porous nanofibers containing well-embedded VN nanodots and highly densified-entangled N-CNTs were synthesized using as-received chemicals. Briefly, Polyacrylonitrile (PAN; M_w = 150000, Sigma-Aldrich), vanadium oxide (V_2O_5, 99.0%, M_w = 181.8, Daejung Chemicals), polystyrene (PS; M_w = 192000, Sigma-Aldrich), CNTs (MWCNTs, length: 10–30 mm, OD: 20–30 nm, Cheap Tubes Inc., Cambridgeport, USA; purity: >95.0 wt%), and urea (NH_2CONH_2, 99.0%, Samchun Chemicals) were utilized. The spinning solution was obtained using *N, N*-dimethylformamide (99.5%, Samchun Chemicals). Hierarchically porous nanofibers comprising N-doped C skeletons with highly densified-entangled N-CNTs and VN nanodots (abbreviated as "P–N–C@VN/N-CNT" NF) were prepared *via* a typical electrospinning process followed by a heating process. In particular, 1.0 g of CNTs were dispersed in DMF (25 mL) solvent using ultrasonication. Before this, the CNTs were purified to remove the metal catalysts or any other impurities using acid treatment. Briefly, the CNTs were dispersed in an HNO_3/H_2SO_4 (1:3 v/v) acidic solution maintained at 80 °C, followed by repetitive washing with ethyl alcohol and distilled water. Consequently, the treated CNTs were freeze-dried and stored until further use. Afterward, 0.7 g of V_2O_5, 1.0 g of oval-shaped PS granules, and 2.0 g of PAN polymer were sequentially added to the DMF solution with continuous stirring. The colloidal solution thus formed was left undisturbed overnight under ambient conditions for homogeneous dispersion. During stirring, a V_2O_5–PAN–CNT complex was produced owing to the dipole-dipole exchange and hydrogen bonding among CNTs and PAN, which resulted in a stable jet during spinning. The prepared spinning solution was put into a syringe pump (volume = 12 mL) equipped with a 21-gauge needle (stainless steel) and electrospun on a drum (rotating at 180 rpm) wrapped with an Al collector. The ejection rate of the solution was fixed at 1.0 mL h^{-1}. The distance and applied voltage between the needle tip and the collector were fixed at 15 cm and 25 kV, respectively. The as-spun V_2O_5/CNT/PS/PAN composite fibers were initially stabilized at 150 °C for 12 h and then at 250 °C for 5 h in an air atmosphere with a ramp rate of 5 °C min^{-1}. Finally, the stabilized composite fibers were exposed to a carbonitrothermic reduction process at 800 °C for 5 h. Urea was used as N-source and the heating was performed under a N_2 atmosphere. The nanofibers thus obtained are abbreviated as P–N–C@VN/N-CNT NFs. For comparison, filled or non-porous PAN-derived nanofibers (F–N–C; F stands for filled), i.e., fibers without V_2O_5, CNTs, and PS, were also prepared using an identical technique followed by a two-step stabilization process at 150 °C (12 h) and 200 °C (1 h) in air atmosphere. The stabilized composite fibers were subsequently heated at 400 °C for 3 h under an N_2 atmosphere.

Characterization Techniques: The morphology and crystal structure analyses of as-prepared P–N–C@VN/N-CNT and F–N–C NF were performed using a Bruker X-ray diffraction (D8) instrument with Cu Kα radiation (λ = 1.5418 Å) at Korea Basic Science Institute (Daegu). The microstructural properties of the prepared nanofibers were examined using Zeiss make field-emission scanning electron microscopy (FE-SEM; UltraPlus) and JEOL make field-emission transmission electron microscopy (JEM-2100F). The thermal endurance of the prepared nanofibers was analyzed using PerkinElmer make thermogravimetric analysis (TGA) (Pyrsis 1) from 25 to 800 °C in an N_2 atmosphere. The heating rate was fixed at 10 °C min^{-1} unless indicated otherwise. The bonding environment of different elements in the prepared nanofibers was determined by Thermo Scientific make X-ray photoelectron spectroscopy (XPS; K-Alpha) coupled with Al Kα X-ray. The specific surface area and pore distribution curves of the as-prepared nanofibers were determined by adsorption-desorption curves based on the Brunauer–Emmett–Teller (BET) method using N_2 as adsorbate gas. The carbon and nitrogen percentage in the samples were determined by an elemental analyzer instrument (EA, Vario MICRO cube). The crystalline properties of carbonaceous products in the as-prepared fibers were examined using the Raman spectroscopy technique (HR800, LabRam, Horiba Jobin-Yvon).

Cell assembly and electrochemical measurements: A slurry-casting method was employed to prepare regular sulfur electrodes as cathodes by mixing active material (elemental S), conductive agent (super-P), and binder (polyvinylidene fluoride; PVDF) in a mass ratio of 7:2:1. *N*-methyl-2-pyrrolidone (NMP) was used as a solvent. The homogeneous slurry was then spread onto an Al collector and dried at 60 °C for 12 h in a hot-air oven. The dried coated slurry was then punched into circular electrodes ($\varphi = 14$ mm). The average active sulfur loading in the electrodes was 1.4 mg cm^{-2}. The active material loading was fixed throughout the electrochemical characterization. The as-prepared P–N–C@VN/N-CNT and F–N–C NF were also coated on a commercial Celgard separator using an identical slurry casting technique and then employed as a multifunctional interlayer. In particular, the as-prepared composite nanofibers, conductive agent, and PVDF binder were thoroughly mixed in a fixed weight ratio (7:2:1), dispersed in a minimum amount of NMP, and stirred for 12 h. The well-dispersed slurry was then coated onto a Celgard separator and dried at 60 °C. The round discs ($\varphi =$ 19 mm) were then punched ($\sim$0.6 mg cm^{-2}) and used as an interlayer. CR2032 coin cells were assembled using sulfur electrodes as a positive electrode, metallic Li as a negative electrode, and coated Celgard separator as a multifunctional interlayer facing toward the cathode. 1.0 M lithium bis(trifluoromethanesulfonyl)imide with 0.5 M $LiNO_3$ in a blend of 1,3-dioxolane (DOL) and 1,2-dimethoxyethane (DME) (1:1, v/v) was used as electrolyte. The electrolyte volume inside the Li–S cell was fixed at 50 μL. The rate capabilities of assembled Li–S cells were measured at different current rates varied from 0.1 C to 2.0 C (1 C was equated to 1675 mA h g^{-1}). The cycling stabilities of the assembled Li–S cells were analyzed at 0.1, 0.5, and 1.0 C. The Cyclic voltammetry (CV) tests were carried out at various scan rates ranging from 0.05 to 0.5 mV s^{-1}. The voltage range throughout the electrochemical characterization was set at 1.7–2.8 V. Electrochemical impedance spectroscopy (EIS) technique was utilized to plot Nyquist plots within a frequency limit of 0.01 Hz–1 MHz using an electrochemical impedance analyzer instrument (ZIVE SP2; WonATech). The amplitude of the AC pulse was fixed at 10 mV.

Polysulfide capturing and catalytic conversion tests: Visual demonstration tests of polysulfide anchoring by the as-prepared composite nanofibers were performed to analyze the polysulfide trapping potential of the prepared nanostructures. Elemental sulfur powder (S, Sigma-Aldrich, 99.98%) and Li_2S ($\geq$99%, Sigma-Aldrich) were dispersed at (5:1 M ratio) in DOL/DME (1:1, v/v) to produce a dark brown Li_2S_6 solution. Afterward, 1.0 mM Li_2S_6 solution was prepared in DOL/DME solvent and dropped into two glass containers having as-prepared nanofibers (5.0 mg each). A standard polysulfide solution was also prepared for comparison. Furthermore, symmetrical cells were made to determine the catalytic effect of the as-prepared nanofibers by using the prepared polysulfide solution. The counter and working electrodes (obtained using the slurry method) were kept identical and separated using a Celgard separator. CV plots were obtained for assembled symmetrical cells at a voltage scan rate of 3.0 mV s^{-1} in a voltage range of −1.0 1.0 V.

3. Results and discussion

The morphological and crystal structural variations of prepared nanofibers were examined after each process to investigate the formation mechanism. The detailed morphologies of the as-spun V_2O_5/CNT// PS/PAN composite fibers obtained after a stabilization step at 150 °C are presented in Fig. 1a–c. The FE-SEM micrograph in Fig. 1a shows a continuous fibrous structure with an average diameter of *ca.* 2 μm. Additionally, the uniform thickness throughout indicates that all constituents were evenly distributed inside the fiber structure without any aggregation. Furthermore, the slightly crumpled surface in Fig. 1b was due to an outward diffusion of the PAN matrix. In addition, the cross-sectional part also revealed the presence of highly densified-entangled CNTs bundles confined inside the structure. In general, the weak van der Waals forces among CNTs tend to induce aggregation, which subsequently results in non-uniform fiber thickness after spinning. Although, in the present study, the acid treatment efficiently prohibited the aggregation of CNTs. It should be noted that CNTs comprise numerous concentric graphene cylinders held together by weak van der Waals forces between the adjacent graphene layers. During acid-treatment, various functional groups get adsorbed on the surface of CNTs which lowers the surface tension thus diminishing the force leading to the formation of aggregates [48]. This process eventually resulted in the formation of uniform precursor complexes in the spinning solution. The XRD pattern of the stabilized nanofibers in Fig. 1c displays sharp peaks that are primarily attributed to the V_2O_5 phase. Besides, a broad XRD peak located at $2\theta = 17.1^\circ$ relates to the PAN matrix in the prepared precursor fibers. The TG curve of the as-spun fibers after stabilization was obtained under N_2 atmosphere to determine the sintering temperature, as presented in Fig. S1. The steep weight loss ($\Delta m_1 = -15.4\%$) between 306 and 322 °C is mainly due to the thermal breakdown of elongated PS phase into gaseous species. A marginal weight loss ($\Delta m_2 = -9.4\%$) between 322 and 408 °C corresponds to the complete removal of PS, along with the beginning of the carbonization process for the PAN matrix. The massive weight loss ($\Delta m_3 = -23.8\%$) between 408 and 450 °C represents the complete conversion of the PAN matrix to the N-doped C framework. However, the slight weight loss from 450 to 800 °C was due to the partial decomposition of the highly densified CNTs. Overall, the TG curve suggests that a heat-treatment temperature $\geq$800 °C would result in the synthesis of a phase-pure composite comprising an N-doped C skeleton with N-CNTs and VN nanodots. Based on the above results, porous composite nanofibers were prepared at an optimized temperature of 800 °C.

The stabilized V_2O_5/CNT/PS/PAN composite fibers were initially subjected to oxidation at 250 °C for 5 h (Fig. 1d–f). The FE-SEM micrograph (Fig. 1d) shows that a continuous fibrous morphology remained intact even after oxidation, with an average diameter of 2.0 μm. The cross-sectional image (Fig. 1e) suggests the partial removal of both PS and AC from PAN matrix, which subsequently resulted in the formation of longitudinal long-range channels and interconnected pores. The porous structure facilitates electrolyte percolation and provides enough space to accommodate the volume changes during the redox processes when employed as an electrode or multifunctional interlayer for LSBs. Moreover, the selective removal of AC increased the overall conductivity of the nanostructures. Notably, during the oxidation process at low temperatures, the highly dense entangled N-CNTs remained intact inside the nanostructure. The XRD pattern in Fig. 1f displays narrow and intense peaks, which are primarily ascribed to the V_2O_5 nanostructure. However, a close inspection showed a broad peak at $2\theta = 25^\circ$, mainly due to the presence of highly-densified-entangled N-CNTs.

Hierarchically porous N–C nanofibers composed of VN nanodots and highly densified entangled N-CNTs (referred as P–N–C@VN/N-CNT NFs) were obtained after the carbonitrothermic reduction reaction of the composite fibers obtained after oxidation at 250 °C. The urea was used as a N source and the heating was performed at 800 °C in N_2 atmosphere.

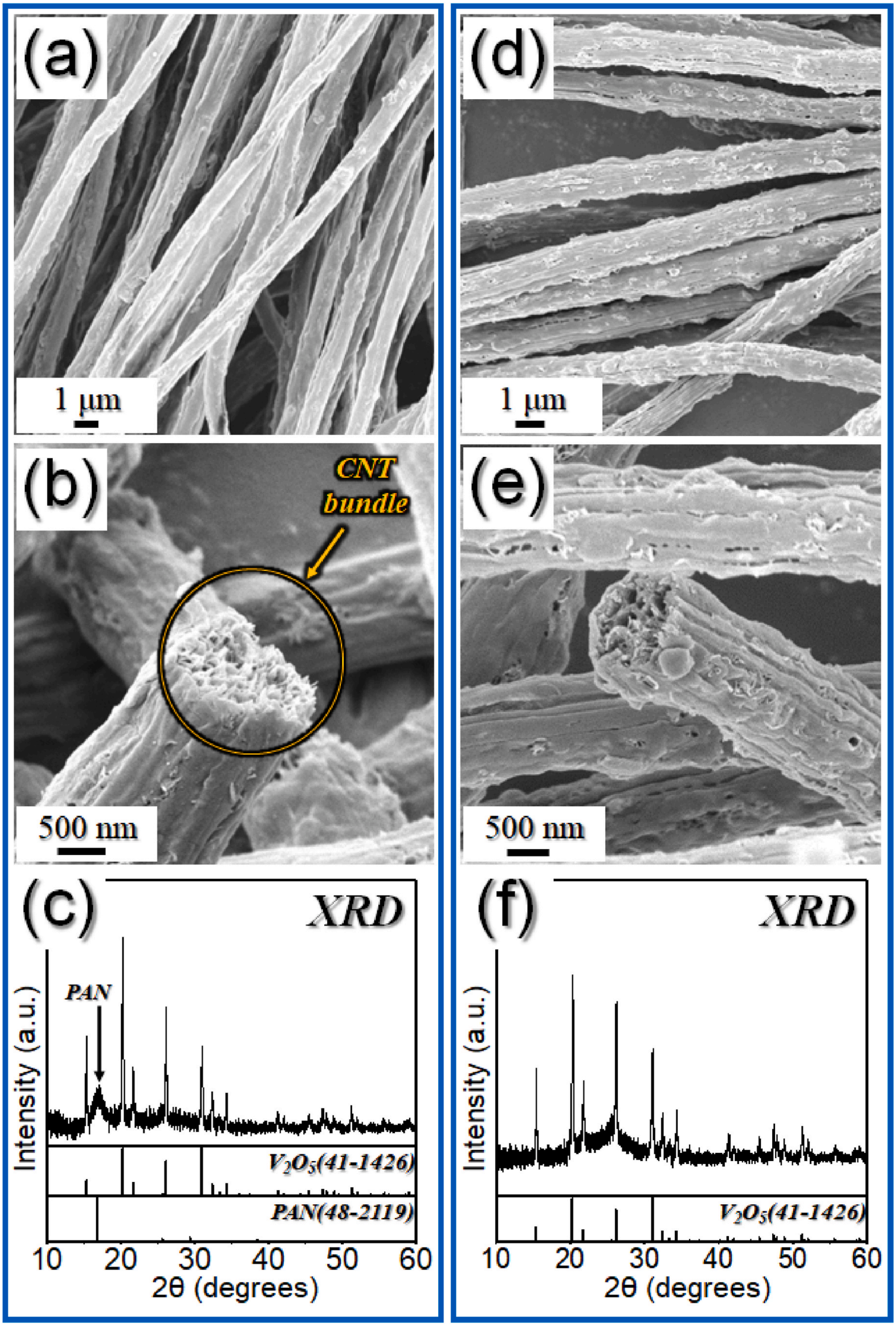

Fig. 1. Morphologies and XRD pattern results of (a–c) V_2O_5/CNT//PS/PAN composite fibers after stabilization at 150 °C and (d–f) V_2O_5/CNT/PS/PAN composite fibers after oxidation at 250 °C: (a, d) FE-SEM images, (b, e) cross-sectional FE-SEM images, (c, f) XRD patterns.

The physical properties of obtained nanofibers are presented in Fig. 2. The FE-SEM micrograph in Fig. 2a reveals a continuous fibrous morphology with an average diameter of *ca.* 1.5 μm. During the high-temperature heat treatment, the residual AC decomposed from the PAN matrix to form N-doped carbonaceous (N-doped C) products. In addition, the residual PS decomposed completely as gaseous products to form porous channels. The uniform thickness of the nanofibers even after heat treatment was apparent, suggesting the non-agglomerated and homogeneous distribution of the metal nitride nanodots and highly densified entangled CNTs inside the nanofiber matrix. The cross-sectional image shown in Fig. 2b firmly supports the above result, with well-formed hollow longitudinal channels due to the removal of the elongated PS phase. The TEM images (Fig. 2c and d) further confirm the continuous fibrous structure of the prepared sample. Furthermore, the high-magnified TEM image in Fig. 2e indicates that the vanadium nitride nanodots (black dots) along with the highly entangled CNTs (indicated by arrows) are well embedded in the N–C framework (grey region). The high-resolution TEM (HR-TEM) image shown in Fig. 2f also indicates well-embedded VN nanodots with well-resolved lattice fringes separated by a distance of 0.21 nm that relates to the (200) diffraction plane. The selected area electron diffraction (SAED) pattern in Fig. 2g shows diffused diffraction rings primarily attributed to the VN phase. Additionally, the diffraction ring corresponding to the highly entangled CNTs (i.e., the (002) plane) is also evident. The XRD pattern in Fig. 2h firmly supports the above results with sharp and intense peaks of VN pure phase besides a broad XRD peak at $\sim 2\theta = 25^\circ$ attributed to the CNTs. The elemental mapping images in Fig. 2i suggest the uniform dispersion of V, N, and C throughout the nanostructure. However, the higher percentage of C element followed by N clearly indicates that the matrix is N-doped C. Overall, the above results indicate the development of hierarchically porous N–C nanofibers comprising well-embedded VN nanodots in the N–C matrix, along with highly densified CNTs.

The comprehensive formation mechanism of the P–N–C@VN/N-CNT NF inferred from the above results is summarized in Scheme 1. In the spinning solution, the non-compatible nature of the PS component results in a dispersed phase mainly due to its different solubility extent than that of PAN polymer [16]. During electrospinning, the dispersed phase of PS formed an island-like structure from the initial oval-shaped structure that stretched along the fiber length under a high electric field (Scheme 1-①). Likewise, acid treatment prohibits the aggregation of CNTs due to van der Waals forces, thus forming homogeneous precursor complexes of V_2O_5/CNT/PAN. During oxidation (Scheme 1-②), both PAN and PS were partially decomposed into AC and removed as gaseous products afterward, which resulted in surface porosity to some extent. However, the CNTs remain intact during this step. The fibers comprising well-embedded V_2O_5 grains, elongated PS along the fiber, and highly densified entangled CNTs were further exposed to a carbonitrothermic process with urea as nitrogen source (Scheme 1-③). During this process, the V_2O_5 grains were reduced to VN nanodots *via* sequential reductive processes ($V^{5+} \rightarrow V^{4+} \rightarrow V^{3+} \rightarrow V^{2+} \rightarrow V^{3+}$ (VN)). In addition, PS decomposes completely to form tunnel-like long-range longitudinal channels. Meanwhile, the residual AC from PAN decomposition was converted to an N-doped C framework comprising well-embedded VN nanodots and grafted N-CNTs. The obtained hierarchically porous nanofibers (P–N–C@VN/N-CNT NFs) were coated on a commercial Celgard separator (Scheme 1-④) and utilized as a multifunctional interlayer.

The chemical states of various elements in the P–N–C@VN/N-CNT NFs were examined using the XPS technique (Fig. 3). The survey spectra (Fig. S2a) clearly indicate the presence of O 1s, V 2p, N 1s, and C 1s photoelectron signals. The magnified V 2p signal (Fig. 3a) indicates five well-fitted deconvoluted peaks. The peak located at 521.6 eV attributed to the presence of VN species in the nanostructure whereas the additional peak pairs located at 514.4/522.1 eV and 516.8/524.1 eV corresponds to the VNO and VO species, respectively, due to the air exposure of P–N–C@VN/N-CNT NF [16,49]. The deconvoluted O 1s XPS spectrum (Fig. 3b) confirms the above results and agrees well with previous reports [50,51]. Furthermore, the deconvoluted C 1s XPS profile (Fig. 3c) indicates four fitted peaks attributed to C═C (284.5 eV), C–N/C–C (285.9 eV), C═O (287.9 eV), and O–C═O (290.6 eV) species [17,52–56]. The most intense C═C peak indicated the existence of a carbonaceous structure in the nanostructure. Additionally, the presence of the C–N/C–C peak implies nitrogen doping in the carbon skeleton, which eventually enhances the overall conductivity due to the high electronegativity of N atom compared to that of C [47]. The deconvoluted N 1s XPS profile (Fig. 3d) exhibits well-fitted peaks at 398.2, 400.8, and 403.9 eV that corresponds to the pyridinic, pyrrolic, and graphitic nitrogen species, respectively, thus confirming the N-doped C framework and firmly supporting the above results [10,57]. The peak centered at 399.2 eV again validates the presence of N species in the VN nanodot nanostructure [58]. Moreover, these results are well authenticated by the EA results presented in Table S1, which indicate a nitrogen content of 8.1 wt% in P–N–C@VN/N-CNT NF. The VN content in the nanostructure was quantify using TG curve (Fig. 3e) and was *ca.* ~39 wt%. The Raman results presented in Fig. 3f indicate an I_D/I_G value of 0.81, implying that the carbonaceous products in the P–N–C@VN/N-CNT NF are mainly graphitic [59,60]. Notably, the formation of graphitic N-doped C during the carbonitrothermic reduction process was mainly derived from partially converted amorphous C (remained after oxidation step), as confirmed by the Raman spectroscopy (Fig. S3).

To validate the structural advantages of P–N–C@VN/N-CNT, filled structured nanofibers comprising only PAN matrix (i.e., without PS, V_2O_5 grains, and CNTs) were also prepared for comparison. After stabilization, the fibers (Figs. S4a and b) showed a continuous solid-type fibrous structure with a mean diameter of ~500 nm. The XRD pattern (Fig. S4c) displays a sharp peak at $2\theta = 17.1^\circ$, which is primarily related to the PAN matrix. The stabilized fibers were then heated at 400 °C in N_2 atmosphere and the obtained morphology is shown in Fig. S5. The FE-SEM micrographs (Figs. S5a and b) showed a smooth surface and filled fibrous structure with a mean diameter of 230 nm. The TEM images (Figs. S5c and d) confirmed that the filled structure was mainly comprised of AC. The SAED pattern (Fig. S5e) with diffused diffraction rings and XRD (Fig. S5f) with a broad diffraction peak at $2\theta = 25^\circ$, suggested amorphous carbonaceous products. Elemental dot mapping images (Fig. S5g) further prove N-doped carbonaceous products. The acrylonitrile group (–C_3H_3N–) in PAN acted as a nitrogen source in the F–N–C NFs. The nitrogen quantification results of F–N–C in Table S1 also suggest a high nitrogen content of 18.7 wt%. The low BET surface area of 14 $m^2\ g^{-1}$ (Fig. S6c) for F–N–C NFs compared to 188 $m^2\ g^{-1}$ for P–N–C@VN/N-CNT NFs (Fig. S6a) further confirm the non-porous structure of the sample. The presence of numerous mesopores (Fig. S6b) originating from the complete decomposition of PS and AC removal resulted in a high surface area for the P–N–C@VN/N-CNT NFs. Overall, the results indicate the successful synthesis of a highly porous and conductive skeleton in the form of N-doped C, along with well-embedded VN nanodots and well-grafted highly densified entangled N-CNTs. The structural advantages of the P–N–C@VN/N-CNT NF envisage enhanced electrochemical performance owing to the presence of enormous conductive and porous channels, which guarantees fast redox kinetics and allows rapid charge diffusion owing to efficient electrolyte penetration. Additionally, the VN nanodots act as active chemisorption sites for effective polysulfide anchoring, thus weakening the shuttling effects and subsequently reducing the active material loss.

The physical properties of the separators coated with the as-prepared nanofibers were also examined (Fig. S7). A digital image of the coated separator (Fig. S7a) indicates a uniform and crack-free coating that resulted in highly integrated circular disks ($\varphi = 19$ mm) to be employed as interlayers (Fig. S7b). The coating thickness was measured using a micrometer and found to be ~10 μm, as shown in the digital photographs (Figs. S7c–e). Furthermore, the excellent mechanical integrity of the coated separator was confirmed by bending and folding operations, as shown in Fig. S7f. The pristine and coated separators were further

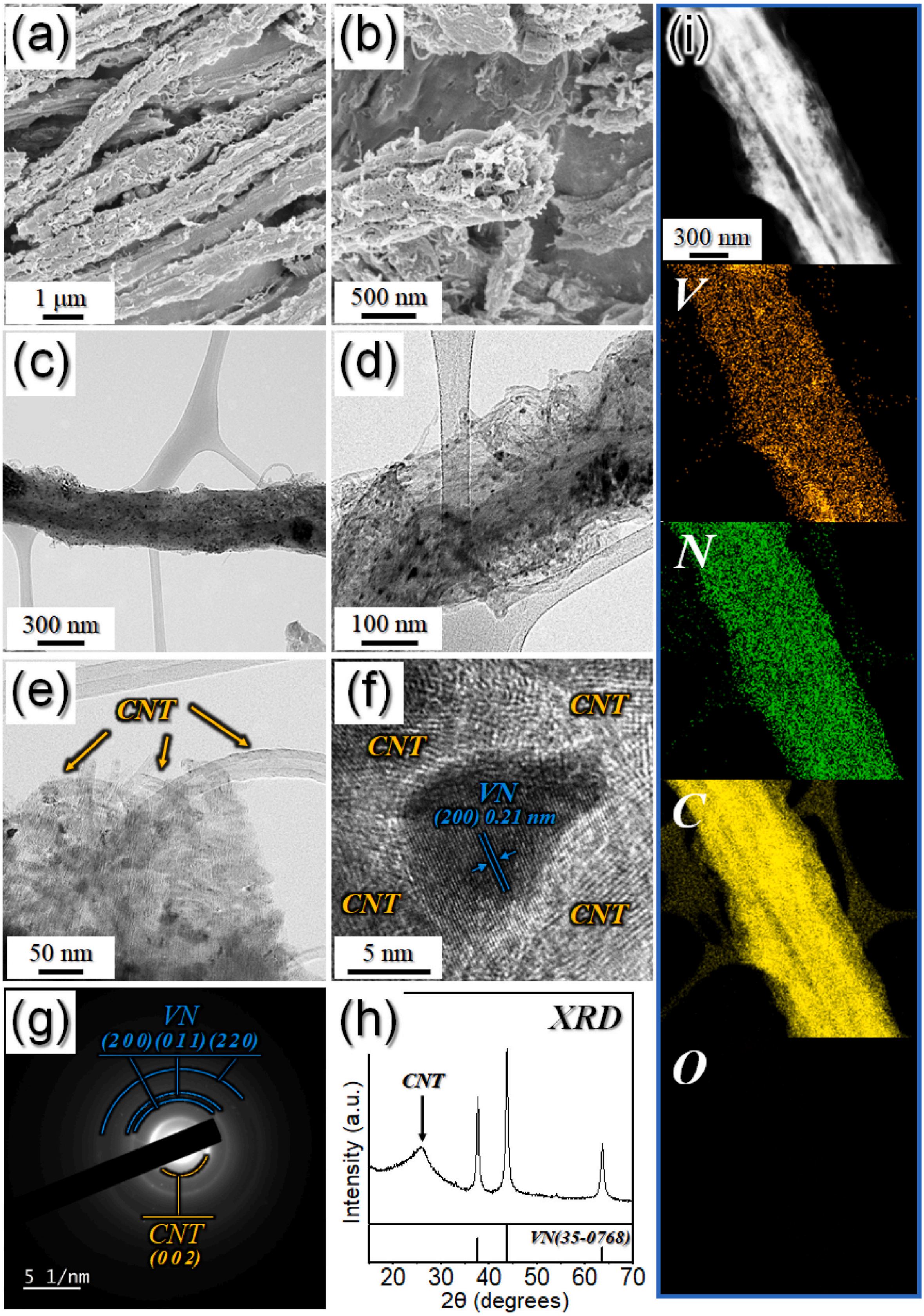

Fig. 2. Characterization of P–N–C@VN/N-CNT NF obtained after carbonitrothermic reduction reaction at 800 °C for 5 h under N_2 atmosphere: (a, b) FE-SEM images, (c–e) TEM images, (f) HR-TEM image, (g) SAED pattern, (h) XRD pattern, and (i) elemental mapping images.

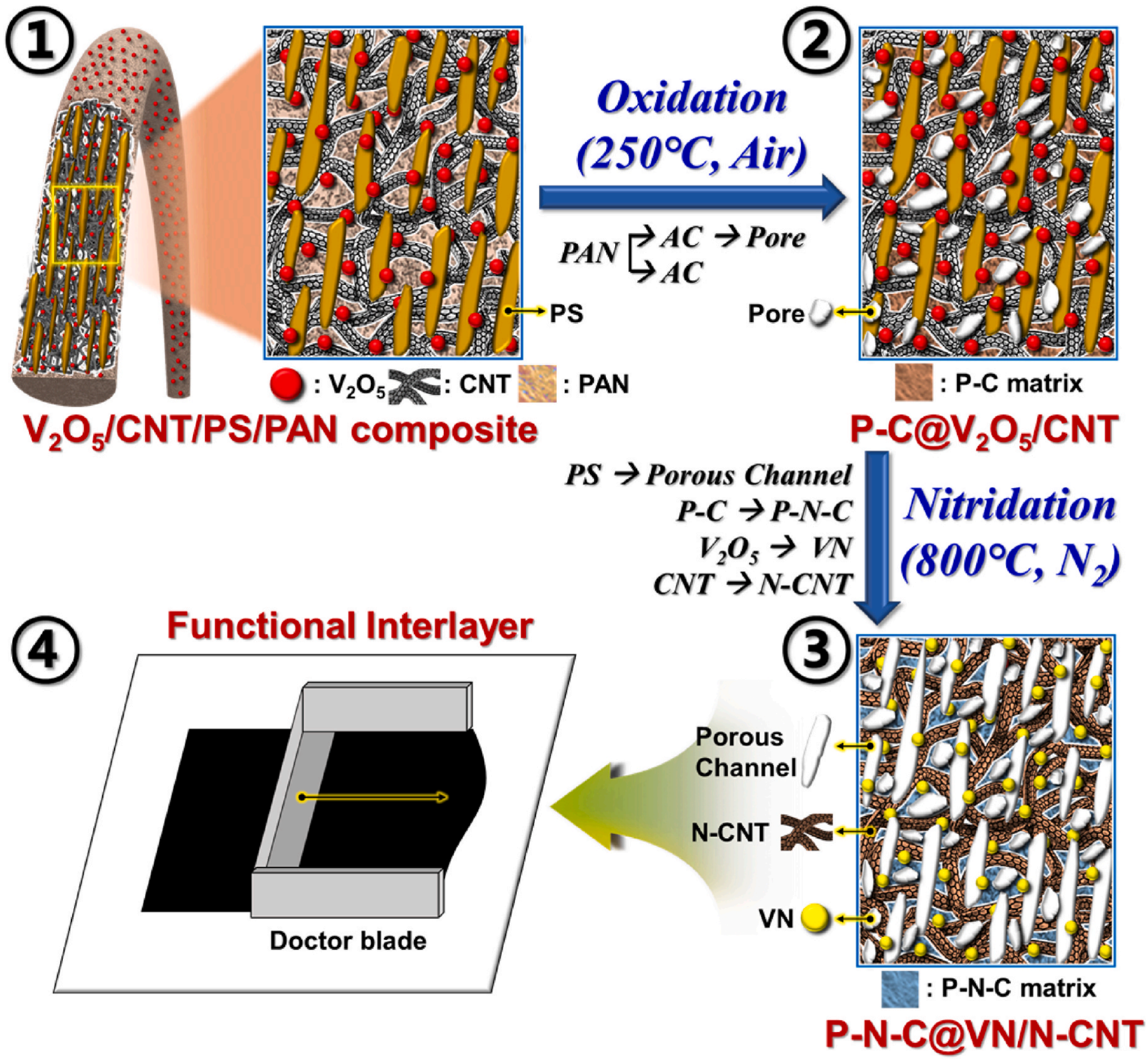

Scheme 1. Schematic elaboration of formation mechanism of hierarchically porous N-doped C nanofibers comprising VN nanodots and densified N-doped CNTs.

examined by microstructural analysis (Fig. S8). The pristine or uncoated Celgard separator (Fig. S8a) showed a nanometer-sized opening that allowed the rapid diffusion of Li–ions during the redox processes. Furthermore, the separator coated with P–N–C@VN/N-CNT NFs clearly indicated a uniform coating of the sample over the Celgard separator surface (Fig. S8b). The coating layer thickness is *ca.* ~10 μm (Fig. S8c) and matches well with the thickness measured in Fig. S7. The above results imply that a uniform coating layer with high mechanical integrity was successfully coated over the Celgard separator for use as a functional interlayer for highly stable LSBs.

The electrochemical performance of Li–S cells utilizing various coated arrangements as functional interlayers is presented in Fig. 4. The Li–S cells were initially exposed to CV tests, as presented in Fig. 4a and Figs. S9a–c. The initial CV curves exhibited well-recognized redox peaks for all assembled Li–S cells featuring various coated separators as interlayers. The initial CV cycle in Fig. 4a exhibits two reduced peaks located at 2.27 and 1.98 V, which correspond to the sequential reduction of sulfur to lower-order insoluble polysulfide through extremely soluble higher- and middle-order lithium polysulfide, respectively, as intermediate products [10]. Additionally, the sharp and broad oxidation peaks observed at 2.43 and 2.56 V, respectively, indicate the successful conversion of insoluble discharge products to sulfur *via* soluble intermediate polysulfides [17]. The relatively higher current intensities for the cell utilizing P–N–C@VN/N-CNT NF in Fig. 4a suggest high specific discharge capacity values compared to those utilizing F–N–C NF coated- or pristine separators. This is well supported by the fact that the cell utilizing the P–N–C@VN/N-CNT NF-coated separator displayed the lowest polarization potential ($\Delta V = 0.15$ V) between the respective CV redox peak pairs compared to the F–N–C NF-coated ($\Delta V = 0.29$ V) and pristine ($\Delta V = 0.35$ V) separators (Fig. 4b). Besides, the CV curves for five initial cycles at 0.1 mV s^{-1} in Fig. S9 exhibit overlapping profiles, indicating extremely reversible redox processes. To authenticate the above results, the Li–S cells were charged–discharged at 0.1 C, as indicated in Fig. 4b. The Li–S cells utilizing the P–N–C@VN/N-CNT NF, F–N–C NF, and pristine separators displayed discharge capacities of 1097, 645, and 568 mA h g^{-1}, respectively. The longer charge–discharge plateau length for the cell featuring the P–N–C@VN/N-CNT NFs indicates better redox kinetics, which is in good agreement with the CV results. Moreover, the higher capacity values for the upper (Q_H) and lower (Q_L) voltage regions for the P–N–C@VN/N-CNT NFs suggest efficient capture and reuse of the S-like species. This was mainly attributed to the well-embedded VN nanodots, which not only act as active chemisorption sites for efficient trapping of polysulfide, thus prohibiting their migration towards the anode, but also guarantee their effective electrocatalytic conversion owing to the high conductivity of VN. In addition, the conductive and porous N–C skeleton provided numerous conductive pathways for fast charge transfer, which subsequently supported kinetically favored redox processes. Overall, the

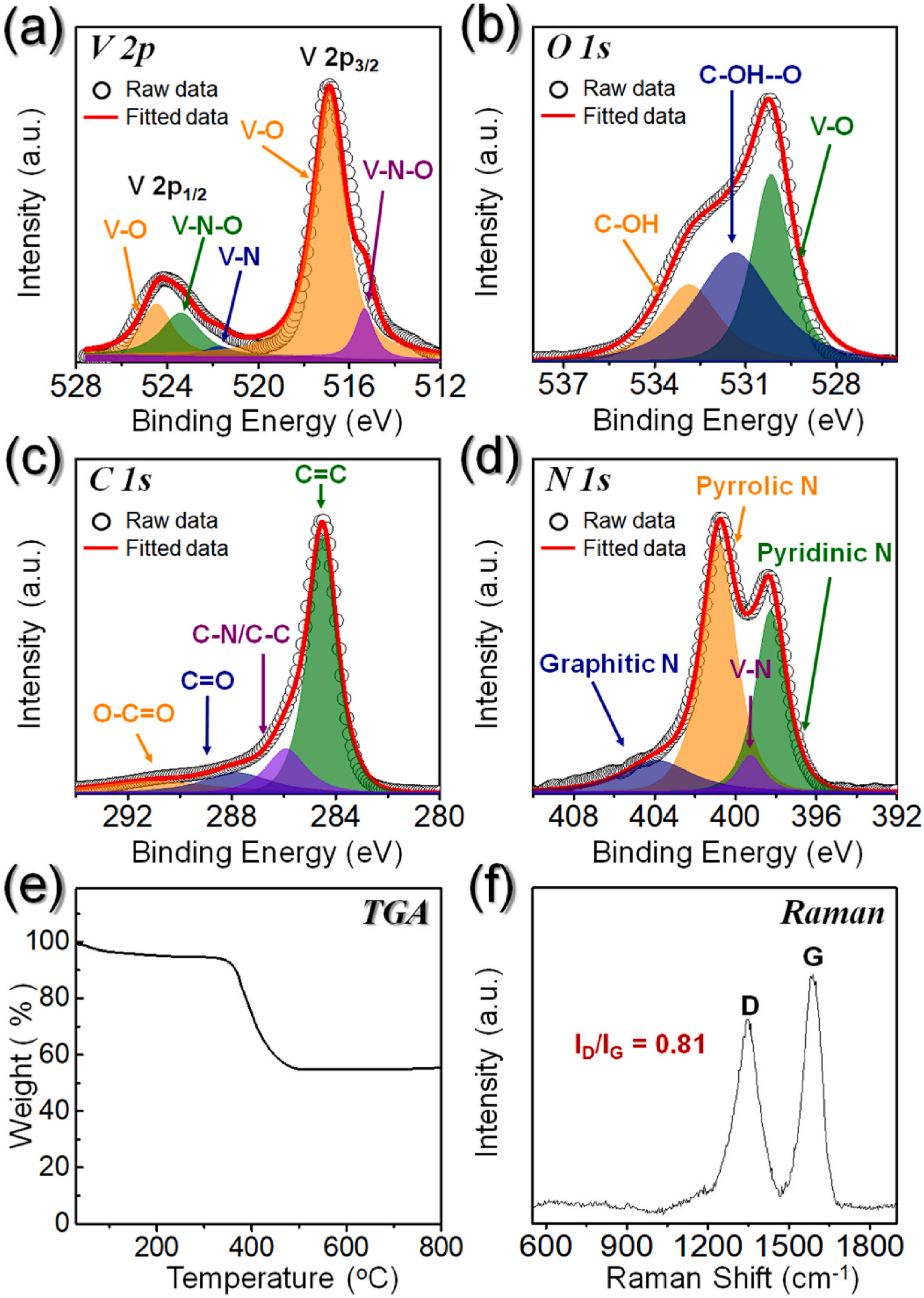

Fig. 3. XPS, TGA curve, and Raman spectrum of P–N–C@VN/N-CNT NF: (a) V 2p XPS spectrum, (b) O 1s XPS spectrum, (c) C 1s XPS spectrum, (d) N 1s XPS spectrum, (e) TG curve, and (f) Raman spectrum.

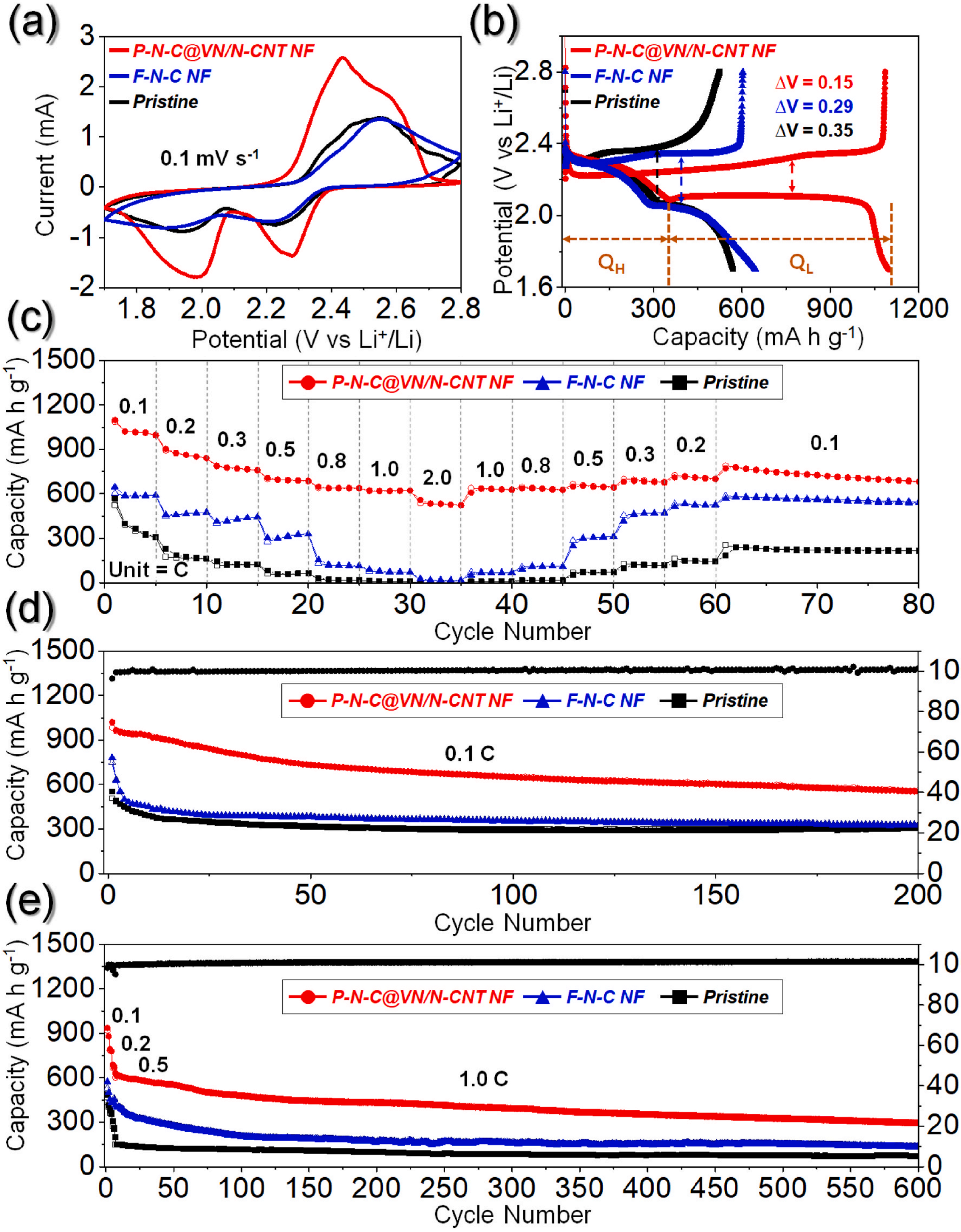

Fig. 4. Electrochemical performances of Li–S cells assembled with different interlayer arrangements: (a) initial CV curves at 0.1 mV s^{-1}, (b) initial charge–discharge voltage profiles at 0.1 C-rate, (c) rate capability test, and cycling performance of the assembled cells at 0.1 C (d) and 1.0 C-rate (e).

above results envisage improved electrochemical performance for P–N–C@VN/N-CNT NFs compared to that of the F–N–C NFs, owing to the synergistic effects of the hierarchically porous and conductive architecture along with the availability of enormous chemisorption sites.

The rate capability tests were conducted at different C-rates ranging from 0.1 to 2.0 C for assembled cells, as indicated in Fig. 4c. The cell employing P–N–C@VN/N-CNT NFs as interlayer displayed initial discharge capacities of 1097, 902, 790, 707, 648, 623, and 559 mA h g^{-1} at 0.1, 0.2, 0.3, 0.5, 0.8, 1.0, and 2.0 C, respectively. In contrast, the cells employing the F–N–C NF interlayer and pristine separators display lower discharge capacities of 645/569, 460/230, 414/145, 303/83, 154/30, 90/13, and 26/0.5 mA h g^{-1}, respectively, at identical rates, confirming the excellent structural merits of the P–N–C@VN/N-CNT NFs. Furthermore, the cell with the P–N–C@VN/N-CNT NF interlayer exhibited a discharge capacity of 772 mA h g^{-1} (~70% of the initial capacity) when the C-rate was reversed to 0.1 C. The reasonable rate capability results are mainly due to the hierarchically porous nanostructure that offers efficient electrolyte infiltration in addition to the conductive N-doped C skeleton that guarantees fast redox processes through rapid electron transfer, and the accessibility of polar sites as highly conductive VN nanodots that allow effective capture of polysulfide species, thus restricting their diffusion towards the anode and hence, improved sulfur utilization. The typical charge–discharge voltage profiles with well-developed long voltage plateaus, especially for the cell employing P–N–C@VN/N-CNT (Fig. S10a) compared to the other interlayer arrangements (Figs. S10b and c) further verified the above results. In addition, capacity utilization curves were also obtained for all the cells in Fig. S11, which confirms that the P–N–C@VN/N-CNT interlayer exhibits the highest sulfur utilization at all C-rates; thus indicating kinetically favored redox processes. Even at a high current of 2.0 C, the cell employing the P–N–C@VN/N-CNT interlayer exhibited a capacity utilization of 44%.

The cycling stability was further examined at 0.1 C-rate, as indicated in Fig. 4d. The cell with P–N–C@VN/N-CNT exhibited an initial discharge capacity of 1020 mA h g^{-1} (~61% of the theoretical capacity). Furthermore, as the cycling proceeded, the capacity stabilized to 552 mA h g^{-1} (~55% capacity retention) after 200 cycles. The prolonged cycling performance of the cell with P–N–C@VN/N-CNT at 0.1 C is presented in Fig. S12a, which implies a discharge capacity of 432 mA h g^{-1} after 400 cycles with an average discharge capacity loss of only 0.14% per cycle. In addition, the high Coulombic efficiency of ~100% indicates that the redox processes are highly reversible. On the other hand, the Li–S cells utilizing the F–N–C NF and pristine separators displayed inferior cycling performance with poor capacity retention. The poor cycling performance of the cell with the F–N–C NFs interlayer was due to the non-accessibility of chemisorption sites along with the non-porous structure which resulted in active-material loss and capacity fading. These results are consistent with the voltage profiles at various cycle numbers of the cells employing different interlayer arrangements, as presented in Fig. S13. Similar cycling performance trends were observed at a high current of 0.5C (Fig. S12b) and 1.0 C-rate (Fig. 4e). The cell featuring P–N–C@VN/N-CNT interlayer retains 60% of the capacity (361 mA h g^{-1}) even after 400 cycles at 0.5 C. Likewise, the Li–S cell utilizing the P–N–C@VN/N-CNT interlayer display high-capacity retention (~46% after 600 cycles) with an average discharge capacity loss of only 0.09% per cycle at 1.0 C-rate. In contrast, the Li–S cells featuring the F–N–C NFs and pristine separators exhibited low-capacity retention over prolonged cycling mainly due to poor reaction kinetics that resulted in low active material utilization as evident from the diminished charge-discharge voltage plateaus in Figs. S13d and f, respectively. The high discharge capacity of the cells with the P–N–C@VN/N-CNT interlayer was attributed to well-resolved charge–discharge plateaus (Fig. S13b). Additionally, the Li–S cell featuring the P–N–C@VN/N-CNT interlayer was also tested to confirm the long-term cycling stability at a high C-rate of 2.0 C, as shown in Fig. S12c. The cell demonstrates an initial discharge capacity of 649 mA h g^{-1} (39% of theoretical value). After 700 cycles, the cell exhibits a discharge capacity of 271 mA h g^{-1} (42% capacity retention) with an average capacity decay rate of 0.08% only. Table S2 compares the electrochemical performance obtained in the present work with those reported previously. The obtained cell performance is either comparable or superior to the previous works. To evaluate the more practical aspect of the prepared interlayer, the Li–S cell featuring the P–N–C@VN/N-CNT interlayer was further exposed to cycling performance at 0.3 C-rate for high-loading regular S electrodes, as shown in Fig. S14. It should be noted that all other parameters remained constant. The Li–S cell displays initial discharge capacities of 757, 694, and 349 mA h g^{-1} at 0.3 C with active material loadings of 2.05, 3.09, and 5.01 mg cm^{-2}, respectively. Even after 250 continuous charge−discharge cycles, the cells retain 65% (492 mA h g^{-1}), 50% (347 mA h g^{-1}), and 94% (329 mA h g^{-1}) of the discharge capacities. These results indicate that even with the high-loading electrodes, the Li–S cells exhibited stable cycling properties. The cycling stability results validate that the structural merits of P–N–C@VN/N-CNT support smooth diffusion of charges during the redox processes and efficiently channelize the volume fluctuations besides effective polysulfide anchoring. A schematic illustration of the modified separator, further describing the role of each component in the prepared nanofibers as an interlayer, is presented in Scheme 2. As indicated, the introduction of a functional interlayer not only guarantees efficient anchoring of the polysulfide species but also enhances the integrity of the regular sulfur cathode, especially for high-loading electrodes.

To authenticate the superior redox kinetics inside the cells featuring P–N–C@VN/N-CNT interlayer, the Li–ion diffusion coefficient (D_{Li}^{+}) was calculated for all cells by analyzing CV measurements at different scan rates from 0.05 to 0.5 mV s^{-1} (Fig. 5). The CV curves exhibited conventional Li–S redox peaks, suggesting that the electrochemical processes inside the cells were between those of elemental S and Li_2S. However, the high peak current intensity for the cell featuring P–N–C@VN/N-CNT NF (Fig. 5a) at all scan rates compared to the other Li–S cells, indicates rapid redox processes along with an efficient diffusion of charges. The well-known Randles–Sevcik equation was further applied to measure the D_{Li}^{+} values for all the cells [10]:

$$I_p = 2.69 \times 10^5 n^{1.5} A\, D_{\mathrm{Li}^+}^{0.5}\, C_{\mathrm{Li}}\, \nu^{0.5} \tag{1}$$

where I_p represents the redox peak current, n is the actual number of electrons during the redox reaction ($n = 2$), A is the electrode area (cm^2), C_{Li} is the concentration (mol L^{-1}) of Li–ion, and v is the voltage scan rate (V s^{-1}). The I_p *vs.* $\nu^{0.5}$ curves obtained for the assembled Li–S cells employing P–N–C@VN/N-CNT NFs, F–N–C NFs, and pristine were shown in Fig. 5b, d, and f, and the corresponding D_{Li}^{+} values all Li–S cells are presented in Table S3. The cell featuring P–N–C@VN/N-CNT NFs exhibited the highest diffusion coefficient values thus indicating superior diffusion kinetics. The diffusion coefficient results again confirm that the synergetic effects between various components in the P–N–C@VN/N-CNT NFs during the design strategy subsequently resulted in an overall improvement in the electrochemical performance compared to the non-porous F–N–C NFs.

The enhanced kinetics inside the assembled cells were further confirmed by Nyquist plots (Fig. 6a). Besides, the obtained Nyquist plots were well-fitted using equivalent circuit model based on series and parallel combination of various parameters (Fig. S15) and all the fitted parameters for different Li–S cells utilizing various coated separators are listed in Table S4. The Li–S cells featuring P–N–C@VN/N-CNT displayed the lowest electrolyte resistance (R_e), even after the 50th cycle, indicating a stable electrode–separator–electrolyte interface. In contrast, the Li–S cells featuring the F–N–C NF interlayer or pristine separator displayed higher R_e values, suggesting relatively slow redox processes. Additionally, the cell utilizing the P–N–C@VN/N-CNT NF exhibited the lowest charge transfer resistance (R_{ct}) compared to the other cells. For instance, at the end of 100th cycle, the cell with P–N–C@VN/N-CNT NF interlayer display an R_{ct} value of only 9.4 Ω compared to 33.7 and 52.7 Ω for the Li–S cells employing F–N–C NF-coated and pristine separators, respectively. Therefore, the above results again advocate that the structural supremacy of the P–N–C@VN/N-CNT NFs not only guarantees smooth redox process but also enhances the structural integrity of the sulfur electrode along with the efficient anchoring of polysulfides.

To further examine the electrocatalytic conversion effect of polysulfide by the P–N–C@VN/N-CNT NFs interlayer, CV curves were obtained using symmetrical cells (Fig. 6b–d). The initial CV profile for symmetrical cells in Fig. 6b exhibit appreciable differences as the P–N–C@VN/N-CNT NF cell displays an effective electrocatalytic behavior towards polysulfides, as apparent from the high current intensity. In contrast, the F–N–C NF symmetrical cell exhibited relatively poor electrocatalytic effects toward lithium polysulfides owing to the absence of active chemisorption sites in the prepared nanofibers. Furthermore, the CV plots for four successive cycles shown in Fig. 6c and d displays almost overlapping curves, suggesting efficient electrocatalytic conversion. These explanations were confirmed by visual

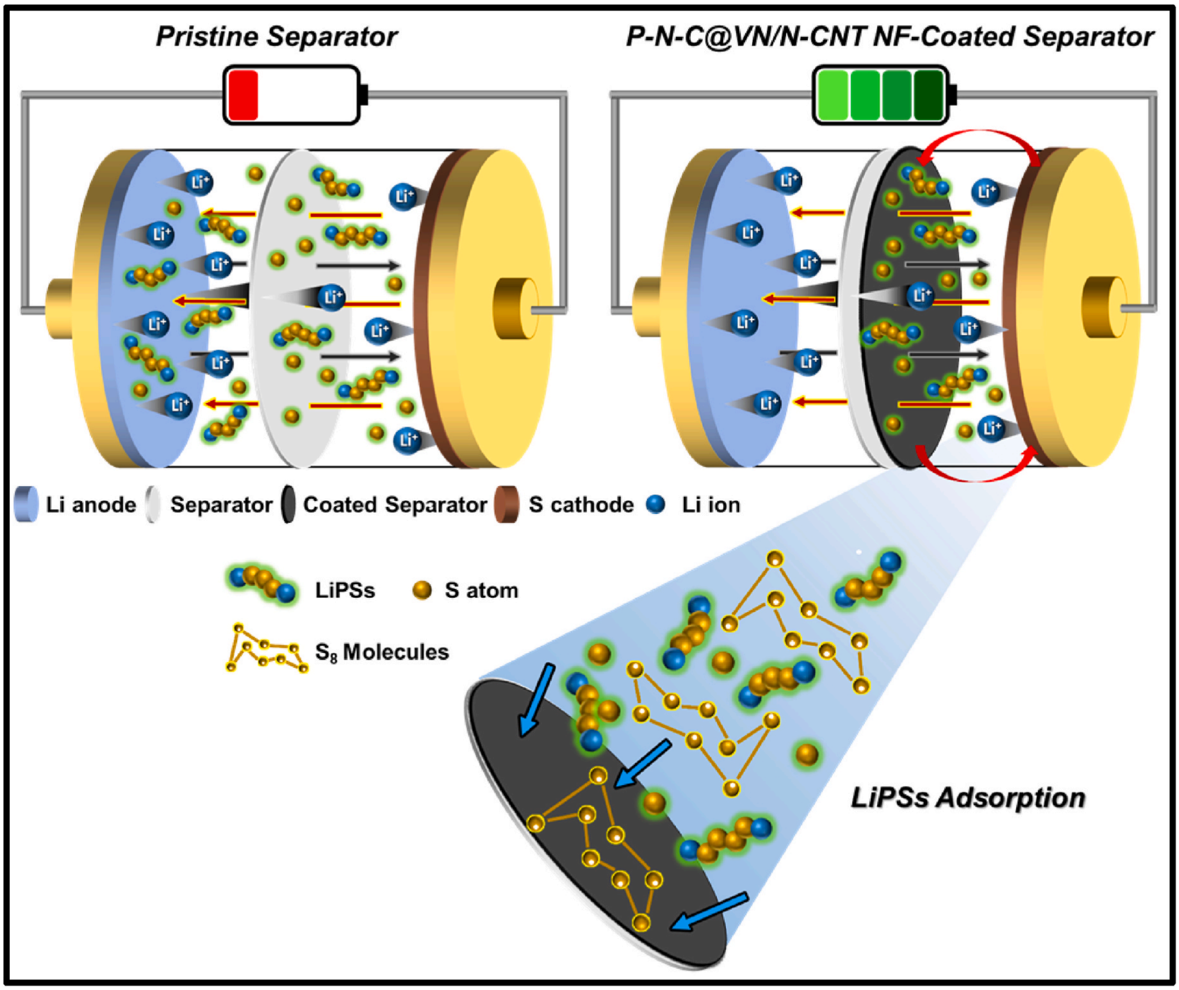

Scheme 2. Schematic illustration elaborating working mechanism of P–N–C@VN/N-CNT NF coated separator for stable Li–S battery.

polysulfide anchoring tests (Fig. 6e). The clear adsorption of lithium polysulfide was apparent from the P–N–C@VN/N-CNT NFs, as indicated by a constant change in the color of the polysulfide solution from yellow at T = 0 to transparent after T = 1 h. In contrast, the solution containing F–N–C NFs displays poor polysulfide adsorption owing to the absence of polysulfide capturing units, as apparent from the slightly yellowish color even after 1 h. Furthermore, the XPS profiles of interlayer materials were also analyzed after cycling for the S 2p photoelectron signal, as shown in Fig. S16. The S 2p XPS profile of commercial sulfur is also presented for better comparison. The two closely spaced peaks at binding energies of 164.5 and 163.4 eV are the characteristic signatures of the S $2p_{1/2}$ and S $2p_{3/2}$ spin-orbit doublet, respectively, in elemental sulfur (S_8) [61,62]. Additionally, the presence of photoelectron signals at binding energies of 166.9 eV for the cycled P–N–C@VN/N-CNT and F–N–C NF is assigned to the thiosulfate (-$S_2O_3^{2-}$) groups [63]. The presence of thiosulfate species is considered as an indication of the surface redox reaction between the polysulfide and VN, which subsequently resulted in the effective mitigation of higher-order polysulfide migration by converting them to insoluble lower-order polysulfides [63]. The broad peak at 168.6 eV is related to the polythionate complexes which formed due to the reaction of elemental S with nucleophilic species such as HS^- or SO_3^{2-} [63]. The polythionate complex is believed to restrict polysulfide shuttling. The fitted peak at 169.9 eV is ascribed to the sulfate (-SO_4^{2-}) species that originated due to LiTFSI decomposition inside the cell which is considered as a key source of Li_xSO_y species [64]. However, the presence of thiosulfate species for F–N–C NF is due to the presence of high N doping in the carbon framework, which also prohibits polysulfide diffusion to some extent due to its high electronegativity. These results clearly validate that the structural merits of the P–N–C@VN/N-CNT NFs resulted in effective capturing/reuse of the polysulfide species owing to the availability of well-embedded VN nanodots as chemisorption sites.

Furthermore, the post-cycling morphology of the cycled separator, shown in Fig. S17 firmly authenticated these results. The FE-SEM micrographs of the cycled separator featuring the P–N–C@VN/N-CNT NFs (Fig. S17a) indicate that the 1D structure remains intact, thus implying the high structural robustness of the nanostructure. In addition, no lithium polysulfide build-up was observed, indicating efficient electrocatalytic conversion of polysulfide species. In contrast, the cells employing the F–N–C NFs (Fig. S17b)-coated separator displayed large lithium polysulfide deposits, suggesting a poor electrocatalytic conversion mechanism due to the non-existence of redox-active sites in the nanostructure. These observations were further strengthened from the morphological characterizations of the S electrodes after cycling, as shown in Fig. S18. The morphology of the S powder in Li–S cells featuring the coated separator arrangements (Figs. S18b and c) resembles pretty well with the uncycled S electrode (Fig. S18a), indicating the enhanced morphological and structural integrity of the active material. However, the S electrode obtained from Li–S cell featuring F–N–C NFs interlayer (Fig. S18c) display higher aggregation compared to the S electrode obtained from Li–S cell featuring P–N–C@VN/N-CNT NFs interlayer (Fig. S18b). Likewise, the morphology of the S powder in Li–S cell utilizing pristine separator (Fig. S18d) exhibits flake-type deposits possibly due to large lithium polysulfides accumulations.

Overall, the introduction of a hierarchically porous and highly

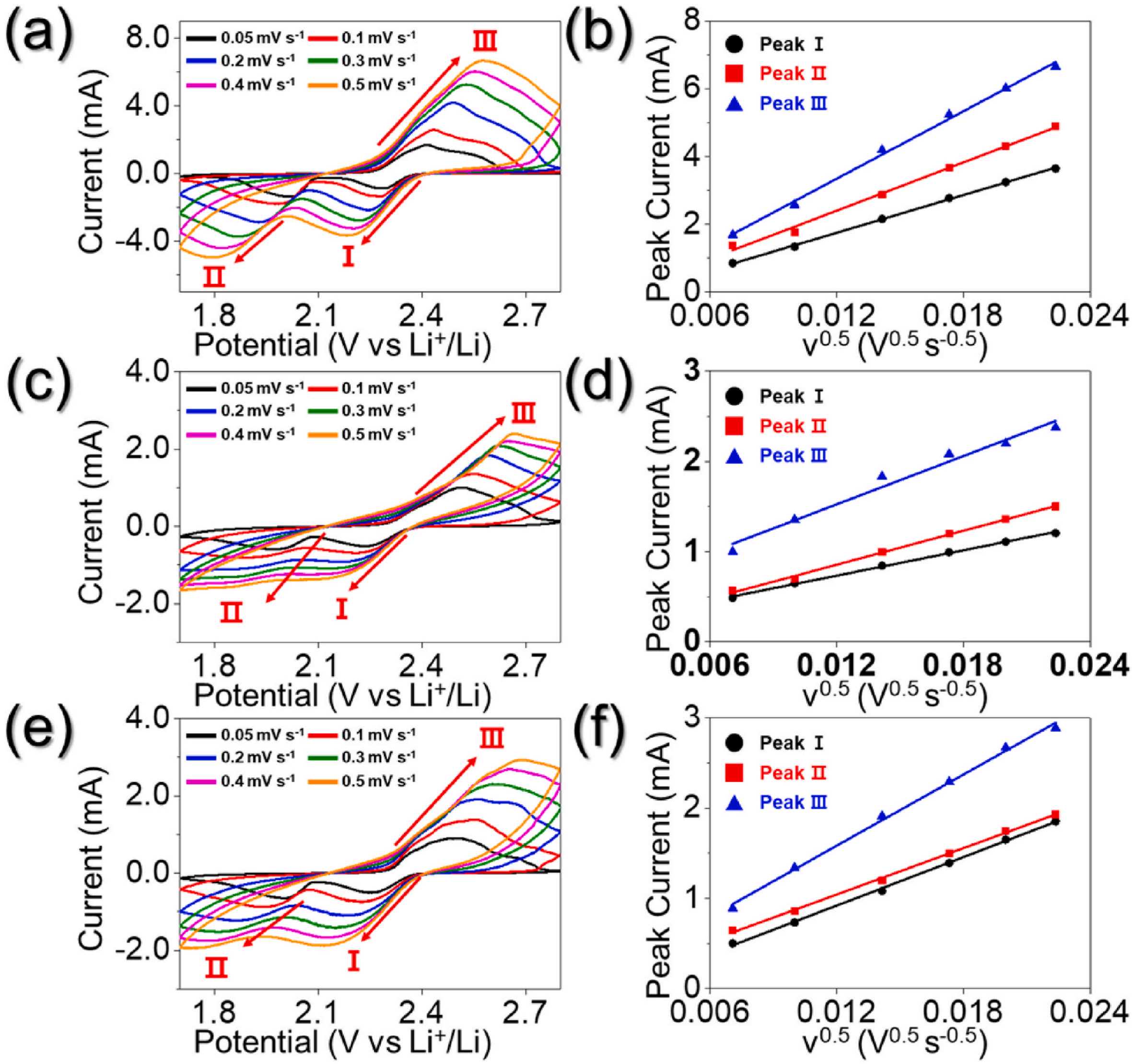

Fig. 5. Lithium–ion diffusion coefficient (D_{Li}^{+}) for the assembled Li–S cells with different interlayer arrangements: (a, b) P–N–C@VN/N-CNT NFs, (c, d) F–N–C NFs, and (e, f) pristine separator.

conductive multifunctional interlayer in the form of a P–N–C@VN/N-CNT NF-coated separator placed on the cathode side demonstrated enhanced electrochemical properties such as decent rate capabilities and prolonged cycling stabilities at various C-rates. The improved cell performance is due to the synergistic effects of the hierarchically porous and conductive N–doped C skeleton, which guarantees rapid charge transfer and better electrolyte percolation. Additionally, the presence of highly conductive and polar VN nanodots allows the effective catalytic conversion of trapped polysulfide species, thus leading to high sulfur utilization. Therefore, we anticipate that the synthesis strategy discussed in this work will substantially enhance the present knowledge on developing conductive and porous nanostructures for various energy-storage applications.

4. Conclusions

In summary, we analyzed the electrochemical performance of Li–S cells by incorporating a modified cell component as coated separator. The multifunctional barrier comprised a hierarchically porous and conductive N–doped C skeleton to support rapid charge diffusion and efficient electrolyte infiltration. In addition, the well-grafted and highly densified entangled N-CNTs increased the overall conductivity. Additionally, the highly conductive vanadium nitride (VN) nanodots act as chemisorption sites for efficient anchoring of polysulfide and prohibit their migration towards the anode through efficient catalytic conversion, thus increasing sulfur utilization. The assembled Li–S cell employing a regular S electrode and a P–N–C@VN@N-CNT NF-coated separator as a polysulfide barrier demonstrated an overall improved electrochemical performance, such as good rate capability (559 mA h g^{-1} at 2.0 C) and stable long-term stability (an average discharge capacity loss of only 0.09% per cycle at 1.0 C-rate after 600 cycles). The physical and electrochemical results discussed in this work will provide considerable insights into the development of porous and conductive nanostructures for various storage applications.

CRediT authorship contribution statement

Jang Min Choi: designed the idea, performed experiments, and prepare initial blueprint. **Rakesh Saroha:** designed the idea, performed experiments, and prepare initial blueprint. **Ji Soo Kim:** carried out experiments. **Mi Rim Jang:** carried out experiments. **Jung Sang Cho:** supervise the work along, Writing – review & editing.

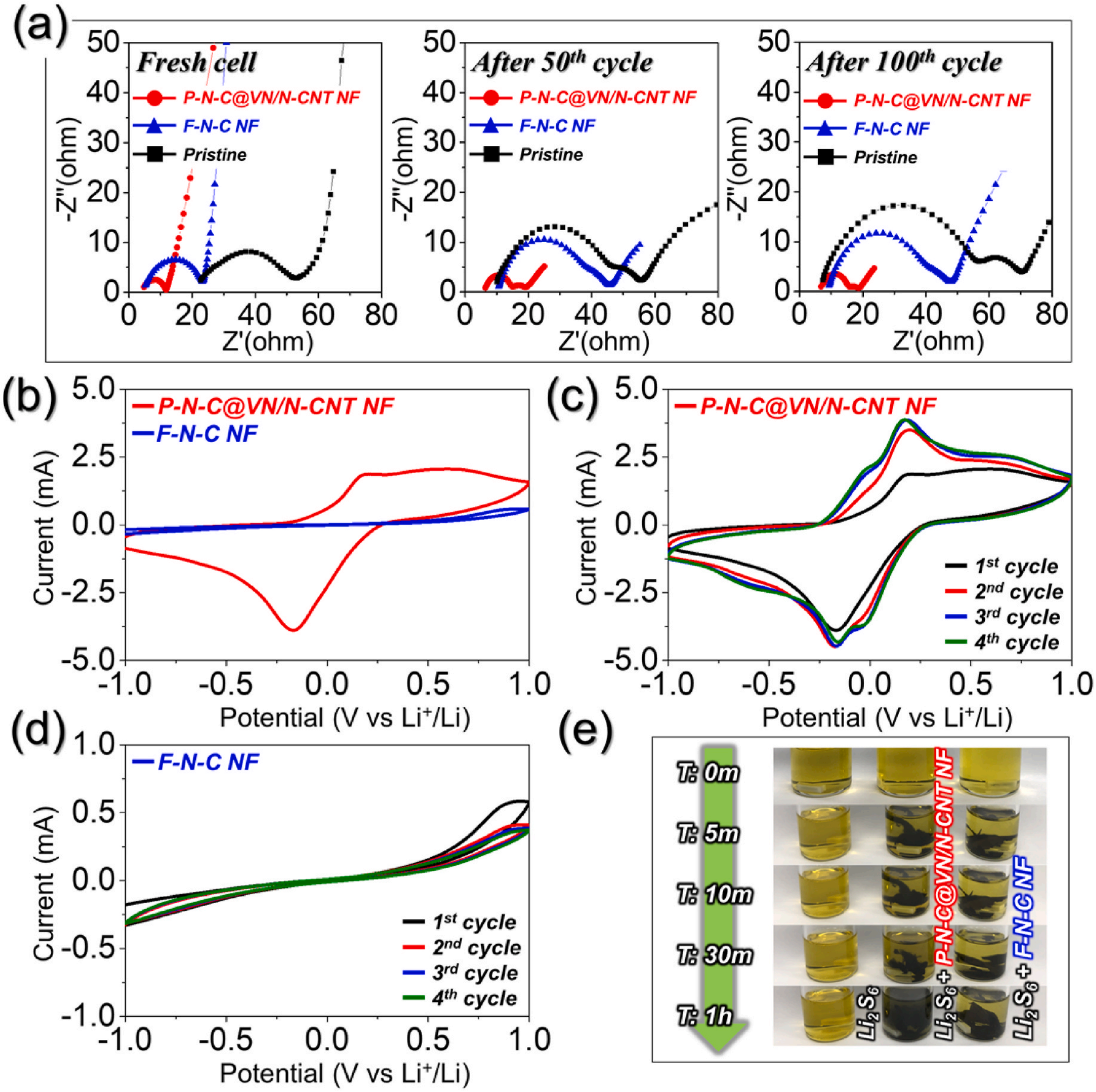

Fig. 6. (a) Nyquist plots at different cycle number at 1.0 C-rate, (b) first CV profile of different symmetric cells in the voltage window of −1.0 to 1.0 V at a scan rate of 3.0 mV s^{-1}, (c, d) first four CV curves obtained using different symmetric cells arrangements, and (e) digital photographs of visual demonstration of polysulfide adsorption tests.

Declaration of competing interest

The authors declare that they have no known competing financial interests or personal relationships that could have appeared to influence the work reported in this paper.

Data availability

No data was used for the research described in the article.

Acknowledgments

This work was supported by the National Research Foundation of Korea (NRF) grant funded by the Korean government (MSIP) (No. NRF-2021R1A4A2001687, and NRF-2021R1I1A3057700. This work was partly supported by Korea Institute of Energy Technology Evaluation and Planning (KETEP) grant funded by the Korea government (MOTIE) (20224000000070, Human Resource Training for Smart Energy New Industry Cluster).

Appendix A. Supplementary data

Supplementary data to this article can be found online at https://doi.org/10.1016/j.jpowsour.2023.232632.

References

[1] R. Saroha, A. Gupta, A.K. Panwar, Electrochemical performances of Li-rich layered-layered Li_2MnO_3-$LiMnO_2$ solid solutions as cathode material for lithium-ion batteries, J. Alloys Compd. 696 (2017) 580–589.

[2] A. Manthiram, Y. Fu, Y.-S. Su, Challenges and prospects of lithium–sulfur batteries, Acc. Chem. Res. 46 (2013) 1125–1134.

[3] R. Saroha, A.K. Panwar, Y. Sharma, P.K. Tyagi, S. Ghosh, Development of surface functionalized ZnO-doped $LiFePO_4$/C composites as alternative cathode material for lithium ion batteries, Appl. Surf. Sci. 394 (2017) 25–36.

[4] R. Saroha, J.S. Cho, J.-H. Ahn, Synergetic effects of cation (K^+) and anion (S^{2-})-doping on the structural integrity of Li/Mn-rich layered cathode material with considerable cyclability and high-rate capability for Li-ion batteries, Electrochim. Acta 366 (2021), 137471.

[5] M. Zhao, B.-Q. Li, X.-Q. Zhang, J.-Q. Huang, Q. Zhang, A perspective toward practical lithium–sulfur batteries, ACS Cent. Sci. 6 (2020) 1095–1104.

[6] R. Saroha, A.K. Panwar, Y. Sharma, Physicochemical and electrochemical performance of $LiFe_{1-x}Ni_xPO_4$ $(0\leq x\leq 1.0)$ solid solution as potential cathode material for rechargeable lithium-ion battery, Ceram. Int. 43 (2017) 5734–5742.

[7] R. Saroha, J.-H. Ahn, J.S. Cho, A short review on dissolved lithium polysulfide catholytes for advanced lithium-sulfur batteries, Kor. J. Chem. Eng. 38 (2021) 461–474.

[8] S. Evers, L.F. Nazar, New approaches for high energy density lithium–sulfur battery cathodes, Acc. Chem. Res. 46 (2013) 1135–1143.

[9] Y.H. Seon, R. Saroha, J.S. Cho, Hierarchically porous N-doped C nanofibers comprising TiO_2 quantum dots and ZIF-8-derived hollow C nanocages as ultralight interlayer for stable Li–S batteries, Compos. B Eng. 237 (2022), 109856.

[10] R. Saroha, J.H. Oh, J.S. Lee, Y.C. Kang, S.M. Jeong, D.-W. Kang, C. Cho, J.S. Cho, Hierarchically porous nanofibers comprising multiple core–shell Co_3O_4@graphitic carbon nanoparticles grafted within N-doped CNTs as functional interlayers for excellent Li–S batteries, Chem. Eng. J. 426 (2021), 130805.

[11] J. Kim, D.J. Lee, H.G. Jung, Y.K. Sun, J. Hassoun, B. Scrosati, An advanced lithium-sulfur battery, Adv. Funct. Mater. 23 (2013) 1076–1080.

[12] M. Hagen, D. Hanselmann, K. Ahlbrecht, R. Maça, D. Gerber, J. Tübke, Lithium–sulfur cells: the gap between the state-of-the-art and the requirements for high energy battery cells, Adv. Energy Mater. 5 (2015), 1401986.

[13] R. Saroha, J. Heo, X. Li, N. Angulakshmi, Y. Lee, H.-J. Ahn, J.-H. Ahn, J.-H. Kim, Asymmetric separator integrated with ferroelectric-$BaTiO_3$ and mesoporous-CNT for the reutilization of soluble polysulfide in lithium-sulfur batteries, J. Alloys Compd. 893 (2022), 162272.

[14] J.-Q. Huang, Q. Zhang, F. Wei, Multi-functional separator/interlayer system for high-stable lithium-sulfur batteries: progress and prospects, Energy Storage Mater. 1 (2015) 127–145.

[15] B. Liu, R. Fang, D. Xie, W. Zhang, H. Huang, Y. Xia, X. Wang, X. Xia, J. Tu, Revisiting scientific issues for industrial applications of lithium–sulfur batteries, Energy Environ. Mater. 1 (2018) 196–208.

[16] R. Saroha, J.H. Oh, Y.H. Seon, Y.C. Kang, J.S. Lee, J.S. Cho, Freestanding interlayers for Li-S batteries: design and synthesis of hierarchically porous N-doped C nanofibers comprising vanadium nitride quantum dots and MOF-derived hollow N-doped C nanocages, J. Mater. Chem. 9 (2021) 11651–11664.

[17] R. Saroha, J.S. Cho, Nanofibers comprising interconnected chain-like hollow N-doped C nanocages as 3D free-standing cathodes for Li–S batteries with super-high sulfur content and lean electrolyte/sulfur ratio, Small Methods (2022), 2200049.

[18] S. Lu, Y. Chen, X. Wu, Z. Wang, Y. Li, Three-dimensional sulfur/graphene multifunctional hybrid sponges for lithium-sulfur batteries with large areal mass loading, Sci. Rep. 4 (2014) 1–4.

[19] Z. Li, Y. Jiang, L. Yuan, Z. Yi, C. Wu, Y. Liu, P. Strasser, Y. Huang, A highly ordered meso@microporous carbon-supported sulfur@smaller sulfur core–shell structured cathode for Li–S batteries, ACS Nano 8 (2014) 9295–9303.

[20] X. Ji, K.T. Lee, L.F. Nazar, A highly ordered nanostructured carbon–sulphur cathode for lithium–sulphur batteries, Nat. Mater. 8 (2009) 500.

[21] Z.-L. Xu, J.-K. Kim, K. Kang, Carbon nanomaterials for advanced lithium sulfur batteries, Nano Today 19 (2018) 84–107.

[22] Z. Sun, J. Zhang, L. Yin, G. Hu, R. Fang, H.-M. Cheng, F. Li, Conductive porous vanadium nitride/graphene composite as chemical anchor of polysulfides for lithium-sulfur batteries, Nat. Commun. 8 (2017) 1–8.

[23] G. Zhou, Y. Zhao, C. Zu, A. Manthiram, Free-standing TiO_2 nanowire-embedded graphene hybrid membrane for advanced Li/dissolved polysulfide batteries, Nano Energy 12 (2015) 240–249.

[24] Z. Li, C. Li, X. Ge, J. Ma, Z. Zhang, Q. Li, C. Wang, L. Yin, Reduced graphene oxide wrapped MOFs-derived cobalt-doped porous carbon polyhedrons as sulfur immobilizers as cathodes for high performance lithium sulfur batteries, Nano Energy 23 (2016) 15–26.

[25] Q. Fan, W. Liu, Z. Weng, Y. Sun, H. Wang, Ternary hybrid material for high-performance lithium–sulfur battery, J. Am. Chem. Soc. 137 (2015) 12946–12953.

[26] H. Yao, G. Zheng, P.-C. Hsu, D. Kong, J.J. Cha, W. Li, Z.W. She, M.T. McDowell, K. Yan, Z. Liang, Improving lithium–sulphur batteries through spatial control of sulphur species deposition on a hybrid electrode surface, Nat. Commun. 5 (2014) 1–9.

[27] Q. Wang, J. Jin, X. Wu, G. Ma, J. Yang, Z. Wen, A shuttle effect free lithium sulfur battery based on a hybrid electrolyte, Phys. Chem. Chem. Phys. 16 (2014) 21225–21229.

[28] R. Saroha, J. Heo, Y. Liu, N. Angulakshmi, Y. Lee, K.-K. Cho, H.-J. Ahn, J.-H. Ahn, V_2O_3-decorated carbon nanofibers as a robust interlayer for long-lived, high-performance, room-temperature sodium–sulfur batteries, Chem. Eng. J. 431 (2022), 134205.

[29] G. Liang, J. Wu, X. Qin, M. Liu, Q. Li, Y.-B. He, J.-K. Kim, B. Li, F. Kang, Ultrafine TiO_2 decorated carbon nanofibers as multifunctional interlayer for high-performance lithium–sulfur battery, ACS Appl. Mater. Interfaces 8 (2016) 23105–23113.

[30] Y. Liu, X. Qin, S. Zhang, G. Liang, F. Kang, G. Chen, B. Li, Fe_3O_4-decorated porous graphene interlayer for high-performance lithium–sulfur batteries, ACS Appl. Mater. Interfaces 10 (2018) 26264–26273.

[31] H. Ahn, Y. Kim, J. Bae, Y.K. Kim, W.B. Kim, A multifunctional SnO_2-nanowires/carbon composite interlayer for high-performance lithium-sulfur batteries, Chem. Eng. J. 401 (2020), 126042.

[32] S.-H. Chung, L. Luo, A. Manthiram, TiS_2–Polysulfide hybrid cathode with high sulfur loading and low electrolyte consumption for lithium–sulfur batteries, ACS Energy Lett. 3 (2018) 568–573.

[33] S. Huang, Y. Wang, J. Hu, Y.V. Lim, D. Kong, Y. Zheng, M. Ding, M.E. Pam, H. Y. Yang, Mechanism investigation of high-performance Li–polysulfide batteries enabled by tungsten disulfide nanopetals, ACS Nano 12 (2018) 9504–9512.

[34] J. Park, B.C. Yu, J.S. Park, J.W. Choi, C. Kim, Y.E. Sung, J.B. Goodenough, Tungsten disulfide catalysts supported on a carbon cloth interlayer for high performance Li–S battery, Adv. Energy Mater. 7 (2017), 1602567.

[35] W. Ren, L. Xu, L. Zhu, X. Wang, X. Ma, D. Wang, Cobalt-doped vanadium nitride yolk–shell nanospheres@carbon with physical and chemical synergistic effects for advanced Li–S batteries, ACS Appl. Mater. Interfaces 10 (2018) 11642–11651.

[36] C. Ye, Y. Jiao, H. Jin, A.D. Slattery, K. Davey, H. Wang, S.Z. Qiao, 2D Mon-VN heterostructure to regulate polysulfides for highly efficient lithium-sulfur batteries, Angew. Chem. Int. Ed. 57 (2018) 16703–16707.

[37] C. Deng, Z. Wang, S. Wang, J. Yu, D.J. Martin, A.K. Nanjundan, Y. Yamauchi, Double-layered modified separators as shuttle suppressing interlayers for lithium–sulfur batteries, ACS Appl. Mater. Interfaces 11 (2018) 541–549.

[38] J. Balach, T. Jaumann, M. Klose, S. Oswald, J. Eckert, L. Giebeler, Functional Mesoporous carbon-coated separator for long-life, high-energy lithium–sulfur batteries, Adv. Funct. Mater. 25 (2015) 5285–5291.

[39] S.H. Chung, A. Manthiram, Bifunctional separator with a light-weight carbon-coating for dynamically and statically stable lithium-sulfur batteries, Adv. Funct. Mater. 24 (2014) 5299–5306.

[40] L. Fan, P. Sun, L. Yang, Z. Xu, J. Han, Facile and scalable synthesis of nitrogen-doped ordered mesoporous carbon for high performance supercapacitors, Kor. J. Chem. Eng. 37 (2020) 166–175.

[41] E. Lim, J. Chun, C. Jo, J. Hwang, Recent advances in the synthesis of mesoporous materials and their application to lithium-ion batteries and hybrid supercapacitors, Kor. J. Chem. Eng. 38 (2021) 227–247.

[42] A. Nulu, V. Nulu, K.Y. Sohn, Silicon and porous MWCNT composite as high capacity anode for lithium-ion batteries, Kor. J. Chem. Eng. 37 (2020) 1795–1802.

[43] S.H. Chung, A. Manthiram, Carbonized eggshell membrane as a natural polysulfide reservoir for highly reversible Li-S batteries, Adv. Mater. 26 (2014) 1360–1365.

[44] Y. Fu, Y.S. Su, A. Manthiram, Highly reversible lithium/dissolved polysulfide batteries with carbon nanotube electrodes, Angew. Chem. Int. Ed. 52 (2013) 6930–6935.

[45] D. Wang, Q. Cao, B. Jing, X. Wang, T. Huang, P. Zeng, S. Jiang, Q. Zhang, J. Sun, A freestanding metallic tin-modified and nitrogen-doped carbon skeleton as interlayer for lithium-sulfur battery, Chem. Eng. J. 399 (2020), 125723.

[46] L. Fan, M. Li, X. Li, W. Xiao, Z. Chen, J. Lu, Interlayer material selection for lithium-sulfur batteries, Joule 3 (2019) 361–386.

[47] J.S. Lee, M.S. Jo, R. Saroha, D.S. Jung, Y.H. Seon, J.S. Lee, Y.C. Kang, D.W. Kang, J. S. Cho, Hierarchically well-developed porous graphene nanofibers comprising N-doped graphitic C-coated cobalt oxide hollow nanospheres as anodes for high-rate Li-ion batteries, Small 16 (2020), 2002213.

[48] R. Atif, F. Inam, Reasons and remedies for the agglomeration of multilayered graphene and carbon nanotubes in polymers, Beilstein J. Nanotechnol. 7 (2016) 1174–1196.

[49] N. Zhang, L. Cao, L. Feng, J. Huang, K. Kajiyoshi, C. Li, Q. Liu, D. Yang, J. He, Co,N-Codoped porous vanadium nitride nanoplates as superior bifunctional electrocatalysts for hydrogen evolution and oxygen reduction reactions, Nanoscale 11 (2019) 11542–11549.

[50] G.-H. An, D.-Y. Lee, H.-J. Ahn, Vanadium nitride encapsulated carbon fibre networks with furrowed porous surfaces for ultrafast asymmetric supercapacitors with robust cycle life, J. Mater. Chem. 5 (2017) 19714–19720.

[51] L. Aissani, M. Fellah, A.H. Chadli, M.A. Samad, A. Cheriet, F. Salhi, C. Nouveau, S. Weiß, A. Obrosov, A. Alhussein, Investigating the effect of nitrogen on the structural and tribo-mechanical behavior of vanadium nitride thin films deposited using RF magnetron sputtering, J. Mater. Sci. 56 (2021) 17319–17336.

[52] J.S. Lee, R. Saroha, S.H. Oh, D.H. Shin, S.M. Jeong, J.K. Kim, J.S. Cho, Rational design of perforated bimetallic (Ni, Mo) sulfides/N-doped graphitic carbon composite microspheres as anode materials for superior Na-ion batteries, Small Methods 5 (2021), 2100195.

[53] C.S. Kim, J.S. Lee, R. Saroha, Y.B. Park, Y.C. Kang, D.-W. Kang, S.M. Jeong, J. S. Cho, Porous nitrogen-doped graphene nanofibers comprising metal organic framework-derived hollow and ultrafine layered double metal oxide nanocrystals as high-performance anodes for lithium-ion batteries, J. Power Sources 523 (2022), 231030.

[54] S.H. Oh, S.M. Park, D.-W. Kang, Y.C. Kang, J.S. Cho, Fibrous network of highly integrated carbon nanotubes/MoO_3 composite bundles anchored with MoO_3 nanoplates for superior lithium ion battery anodes, J. Ind. Eng. Chem. 83 (2020) 438–448.

[55] J.S. Lee, R. Saroha, J.S. Cho, Porous microspheres comprising $CoSe_2$ nanorods coated with N-doped graphitic C and polydopamine-derived C as anodes for long-lived Na-ion batteries, Nano-Micro Lett. 14 (2022) 1–22.

[56] J.S. Lee, R. Saroha, J.H. Oh, C. Cho, B. Jin, D.-W. Kang, J.S. Cho, Camphene-derived hollow and porous nanofibers decorated with hollow NiO nanospheres and graphitic carbon as anodes for efficient lithium-ion storage, J. Ind. Eng. Chem. 114 (2022) 276–287.

[57] R. Saroha, Y.H. Seon, B. Jin, Y.C. Kang, D.-W. Kang, S.M. Jeong, J.S. Cho, Self-supported hierarchically porous 3D carbon nanofiber network comprising Ni/Co/$NiCo_2O_4$ nanocrystals and hollow N-doped C nanocages as sulfur host for highly reversible Li–S batteries, Chem. Eng. J. 446 (2022), 137141.

[58] Y. Yang, K. Shen, Y. Liu, Y. Tan, X. Zhao, J. Wu, X. Niu, F. Ran, Novel hybrid nanoparticles of vanadium nitride/porous carbon as an anode material for symmetrical supercapacitor, Nano-Micro Lett. 9 (2017) 6.

[59] R. Saroha, A.K. Panwar, Effect of in situ pyrolysis of acetylene (C_2H_2) gas as a carbon source on the electrochemical performance of $LiFePO_4$ for rechargeable lithium-ion batteries, J. Phys. D Appl. Phys. 50 (2017), 255501.

[60] R. Saroha, H.S. Ka, J.S. Cho, A novel three-dimensional mesoporous microspheres comprising N-doped graphitic carbon-coated Fe_xP nanoparticles as multifunctional

interlayers to suppress polysulfide crossover in Li–S batteries, Appl. Surf. Sci. 612 (2023), 155892.

[61] L. Qie, W. Chen, X. Xiong, C. Hu, F. Zou, P. Hu, Y. Huang, Sulfur-doped carbon with enlarged interlayer distance as a high-performance anode material for sodium-ion batteries, Adv. Sci. 2 (2015).

[62] H. Cai, Y. Xia, C. Dao, J. Li, L. Lin, X. Kong, S. Chen, Z. Huang, G. Chen, Ambient-air sulfurization process for Cu_2ZnSnS_4 thin film solar cells: self-creating inert atmosphere using sulfur vapor, ACS Appl. Energy Mater. 2 (2019) 7279–7287.

[63] X. Liang, C. Hart, Q. Pang, A. Garsuch, T. Weiss, L.F. Nazar, A highly efficient polysulfide mediator for lithium–sulfur batteries, Nat. Commun. 6 (2015) 1–8.

[64] V. Sharova, A. Moretti, T. Diemant, A. Varzi, R.J. Behm, S. Passerini, Comparative study of imide-based Li salts as electrolyte additives for Li-ion batteries, J. Power Sources 375 (2018) 43–52.